This is a repository copy of *Transmission Electron Microscopy Reveals Deposition of Metal Oxide Coatings onto Metal-Organic Frameworks.*.

White Rose Research Online URL for this paper:
http://eprints.whiterose.ac.uk/126902/

Version: Accepted Version

1
2
3
4
5
6
7
8
9
10
11
12
13
14
15
16
17
18
19
20
21
22
23
24
25
26
27
28
29
30
31
32
33
34
35
36
37
38
39
40
41
42
43
44
45
46
47
48
49
50
51
52
53
54
55
56
57
58
59
60

Transmission Electron Microscopy Reveals Deposition of Metal Oxide Coatings onto Metal-Organic Frameworks

Michael S. Denny, Jr.[1],[†] Lucas R. Parent[1,2,3,4],[†] Joseph P. Patterson[1.5] Santosh Kumar Meena[1], Huy Pham[1], Patricia Abellan[6], Quentin M. Ramasse[6], Francesco Paesani[1], Nathan C. Gianneschi[1,2,3,4],[*] and Seth M. Cohen[1],[*]

[1]Department of Chemistry & Biochemistry, University of California, San Diego, La Jolla, CA 92093. [2]Department of Chemistry, Northwestern University, Evanston, IL 60208. [3]Department of Materials Science & Engineering, Northwestern University, Evanston, IL 60208. [4]Department of Biomedical Engineering, Evanston, IL 602089, Laboratory of Materials and Interface Chemistry and Center of Multiscale Electron Microscopy, [5]Department of Chemical Engineering and Chemistry, Eindhoven University of Technology, Eindhoven, The Netherlands. [6]SuperSTEM Laboratory, SciTech Daresbury Campus, Daresbury, UK.

Supporting Information Placeholder

ABSTRACT: Postsynthetic strategies for modifying metal-organic frameworks (MOFs) have proven to be an incredibly powerful approach for expanding the scope and functionality of these materials. Previously, we reported on the postsynthetic exchange (PSE) of metal ions and ligands in the University of Oslo (UiO) series of MOFs. Detailed characterization by several analytical methods, most notably inductively coupled plasma mass spectrometry (ICP-MS) and transmission electron microscopy (TEM) reveal that metal ion deposition on the surface of these MOFs occurs in the form of nanoscale metal oxides, rather than yielding exchanged metal sites within the MOFs, as was previously reported. By contrast, these combined analytical methods do confirm that ligand-based PSE can occur in these MOFs. These findings provide new insight into the postsynthetic manipulation of MOF materials, highlight the importance of rigorously characterizing these materials to correctly assign their composition and structure, and provide a new route to making hybrid solids with a MOF@metal oxide architecture.

INTRODUCTION

The scope of metal-organic framework (MOF) research has continued to grow as more applications of these porous, crystalline materials are explored,[1-4] including efforts to employ MOFs as heterogeneous catalysts.[5-8] Many MOFs are amenable to postsynthetic processing as a means to modify the native composition to yield materials with functionality and properties not present in the parent MOF.[9-11] Processes like postsynthetic modification (PSM) and postsynthetic exchange (PSE; also referred to as solvent assisted ligand exchange, or SALE) are among the most popular postsynthetic processing methods.[10, 12-13] PSE of metals at the inorganic nodes, known as secondary building units (SBUs; Figure 1), of the MOF has been used to access MOFs that do not form natively with certain metal ions, but often can add stability or enhanced functionality to the framework over other forms.[13-15]

One of the earliest metal-based PSE processes reported was the exchange of Zr^{4+} for Hf^{4+} or Ti^{4+} in the SBU of the UiO-66(Zr)[16] system.[17-19] The Ti^{4+} PSE species is particularly intriguing because UiO-66(Ti) cannot be synthesized directly, but UiO-66(Zr/Ti) generated by PSE has been shown to display enhanced catalytic activity for the reduction of carbon dioxide.[20-25] This system is somewhat unique because the UiO-66 node is both highly stable and interconnected, where many other metal PSE processes involve less stable, or more highly exposed SBUs.[15] Each Zr^{4+} site in the UiO-66(Zr) SBU is eight-connected, bound to 1,4-benzene dicarboxylate (bdc^{2-}) ligands, intracluster bridging oxo ligands, and terminal water/hydroxide groups.
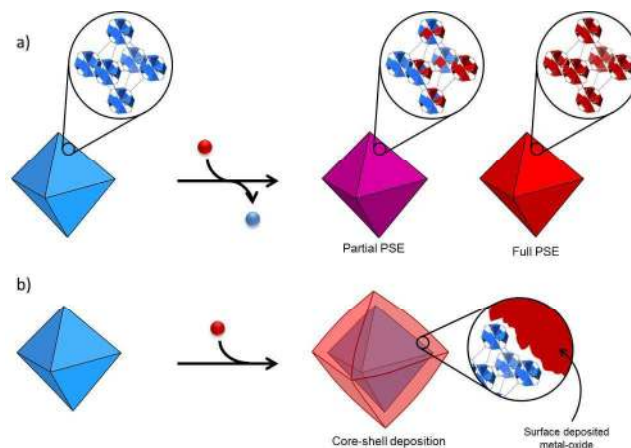
Figure 1. a) The presumed mechanism of postsynthetic exchange (PSE) is a process of displacement of Zr^{4+} ions in the MOF SBU with exogenous metal ions from solution. PSE may consist of partial or full replacement of the native Zr^{4+} ions (blue) with the exogenous metals (red). b) The metal oxide deposition process described here following the addition of exogenous Ti^{4+} and Hf^{4+} occurs at the surface of UiO-66 particles, giving a core-shell, MOF@metal oxide, structure.

Given the opportunity to both improve our fundamental understanding of this exchange process and the utility of this PSE reaction, we sought to study the metal PSE process with both Ti^{4+} and Hf^{4+} by high-resolution transmission electron microscopy (TEM). Using scanning (S)TEM with energy dispersive X-ray spectroscopy (STEM-EDX) and electron energy loss spectroscopy (STEM-EELS), high resolution maps of the exchanged samples were obtained. Curiously, these analyses revealed that a wholly different phenomenon was occurring in the PSE processing of these materials. The resulting MOFs were not exchanging Zr^{4+} at the SBUs, but rather having metal oxides deposited as nanoscale coatings on the MOF surfaces (**Error! Reference source not found.**). This finding is consistent with and related to a recent report describing grafting of Ti^{4+} to the SBU of UiO-66(Zr).[26] The use of high-resolution, analytical STEM revealed that what was originally proposed as PSE, based on other, standard analytical methods and alternative techniques, was actually a metal oxide deposition process masquerading as PSE.[17-19] This discovery of nanoscale HfO_2 and TiO_2 coatings on UiO-66(Zr), as well as ZrO_2 coatings on UiO-66(Hf), suggests that analysis by STEM spectroscopy should be adopted as a more common protocol for MOF systems,[27-28] especially those that appear to display metal-based PSE.

EXPERIMENTAL SECTION

General Information. Starting materials and solvents were purchased and used without further purification from commercial suppliers (Sigma-Aldrich, Alfa Aesar, EMD, TCI, and others). Details of MOF syntheses and postsynthetic protocols are provided in the electronic supporting information (ESI).

Powder X-Ray Diffraction (PXRD). ~50 mg of MOF powder was mounted on a silicon sample holder for analysis by PXRD. PXRD data were collected at ambient temperature on a Bruker D8 Advance diffractometer at 40 kV, 40 mA for Cu Kα radiation (λ = 1.5418 Å), with a scan speed of 2 sec/step, a step size of 0.02° in 2θ, and a 2θ range of 4-50°.

Surface Area Analysis. Samples for analysis were evacuated on a vacuum line overnight at room temperature prior to analysis. ~50 mg of MOF were then transferred to pre-weighed sample tubes and degassed at 105 °C on a Micromeritics ASAP 2020 Adsorption Analyzer for a minimum of 12 h or until the outgas rate was <5 mmHg. After degassing, the sample tubes were re-weighed to obtain a consistent mass for the samples. Sorption data and Brunauer-Emmett-Teller (BET) surface area (m^2/g) measurements were collected at 77 K with N_2 on a Micromeritics ASAP 2020 Adsorption Analyzer using the volumetric technique.

Scanning Electron Microscopy (SEM-EDX). MOFs were transferred to conductive carbon tape on a sample holder disk, and coated using a Ir-sputter coating for 9 sec. A Philips XL ESEM instrument was used for acquiring images using a 10 kV energy source under vacuum at a working distance at 10 mm. Energy dispersive X-ray spectroscopy (EDX) spectra were obtained for the samples via the attached Oxford EDX system.

Nuclear Magnetic Resonance Spectroscopy (NMR). Proton nuclear magnetic resonance spectra (^{1}H NMR) were recorded on a Varian FT-NMR spectrometer (400 MHz). Chemical shifts are quoted in parts per million (ppm) referenced to the appropriate solvent peak or 0 ppm for TMS. MOFs were digested for NMR analysis by immersion of ~8-10 mg of MOF in 590 μL DMSO-d_6 with 10 μL HF (48% in water) with bath sonication at room temperature.

Thermogravimetric analysis and differential scanning calorimetry (TGA/DSC). ~10 mg of MOF sample were taken directly from N_2 gas sorption analysis and placed in a 70 μL alumina crucible. The samples were analyzed on a Mettler Toledo Star TGA/DSC using a temperature range of 30-800 °C scanning at 5 °C/min under an N_2 atmosphere (75 cm^3/min N_2 flow rate).

Inductively Coupled Plasma Mass Spectrometry (ICP-MS). ICP-MS measurements were recorded on Thermo Scientific iCAP™ RQ ICP-MS. The samples were prepared for analysis by dissolution of ~5 mg of MOF with HF (10 μL, 48% in water; ≥ 99.99% trace metals) in 1 mL of DMSO (ACS grade). The samples were then diluted for analysis with 2% HNO_3 (trace grade) in water (≥17.0 MΩ).

TEM Sample Preparation. The same preparation was used for all MOF samples. A small mass (~0.1 mg) of MOF powder was added to 70 μL MeOH and the solution was sonicated until no visible solid material remained (~20-40 min) and the solution became turbid and opaque. 4 μL of the sonicated MOF in MeOH solution was transferred by pipette onto the carbon side of lacey-carbon grids (Electron Microscopy Sciences, Hatfield, PA. Cu mesh supports were used for the UiO-66 samples, and Ni mesh supports for the Zn(Cu)-MOF and UiO-66(Zr) + I-H_2bdc samples. The solution droplet sat on the grid surface for ~20-30 s under ambient conditions, and was then wicked dry with filter paper. The MOF-grids were then stored in a grid box for ~1 week prior to TEM analysis.

STEM Energy Dispersive X-ray Spectroscopy (EDX). All EDX spectra and high-angle annular dark-field (HAADF) STEM images associated with the EDX spectral maps (Figures 4, 7, 9, 10, and Figure S43) were acquired using an FEI Titan located at Pacific Northwest National Laboratory (PNNL-EMSL). The FEI Titan operated at 300 kV (field-emission gun), using a ~5 Å diameter electron probe and an average beam current of ~0.7-1 nA (as measured on the large phosphorous screen through vacuum): 4500 V FEG extraction, 90 μA FEG emission, spot size 3, 70 μm CL aperture, gun lens 3, 300 mm camera length, ~20.9-80 mrad semi-angular range of the annular dark field detector. The FEI Titan was equipped with an EDAX X-ray spectrometer (Ametek, Inc., Berwyn, PA, model PV97-61850 ME, active area 30 mm^2, collection angle ~0.09 srad), and the sample rod was rotated to +17° to maximize X-ray signal collected by the EDX spectrometer. FEI TIA software was used for EDX spectral mapping: 5 eV/channel dispersion at 102.4 μs (range: 0-20 keV), with drift correction set to 1 image/slice, and 1 slice/reference (using MCF correlation function drift correction). Sub-pixel scanning was not used when acquiring EDX spectral maps. The probe dwell location was positioned at the center of each pixel in the STEM EDX maps. Each EDX spectrum (Figures 4, 7, 9, 10, and Figure S43) was acquired using either 500, 700, or 1,000 s dwell-time. Dwell time was adjusted for each particle being analyzed depending on EDX signal generated; for lower signal, a longer dwell-time was used. Details on the EDX Quantification and the creation of the EDX elemental maps can be found in the ESI. Images of all the samples after STEM-EDX map acquisition are provided in Figure S90.

STEM Electron Energy Loss Spectroscopy (EELS). All EELS spectra and HAADF STEM images associated with the EELS spectral maps (Figure 5) were acquired using a Nion UltraSTEM 100 operating at 100 kV (cold field-emission gun), using a ~0.1 nm diameter electron probe and an average beam current of ~13pA (convergence semi-angle 32 mrad, collection semi-angle 37 mrad, 1mm, HAADF semi-angular range ~80-185 mrad). The microscope, located at the SuperSTEM Laboratory (UK), was equipped with a Gatan Enfina GIF spectrometer (Gatan Inc., Pleasanton, CA). EELS maps in Figure 5 were acquired using 0.045 s exposure (per pixel) in Figure 5c, d (34×38 pixels), 0.1 s exposure (per pixel) in Figure 5f, g (60×85 pixels), and 0.5 s exposure (per pixel) in Figure 5j-l (15×158 pixels). The spectrometer dispersion was adjusted to 0.3 eV/channel in order to collect EELS signal over a 402 eV range, allowing for the C, O, and Ti signals to be recorded simultaneously. Vertical binning (100x) was used for all measurements, while spectrum binning

2

(2x) was used for the spectrum image (SI) maps in Figure 5j-l to improve signal-to-noise. To generate the EELS maps for relative element signal, Gatan DigitalMicrograph (DM) software was used to apply standard (power law) background extraction and subtraction to all spectra prior to signal integration A 278.8-325.3 eV energy window was used for carbon mapping (Figure 5c, f, j), a 529.6-550.9 eV energy window was used for oxygen mapping (Figure 5d, g, k), and 452.1-471.2 eV energy window was used for titanium mapping (Figure 5l). Each map was then visualized by applying the "temperature" coloration using the DM software. The fast Fourier Transforms (FFT) of the STEM images in Figure 5 were created using Fiji ImageJ software (http://imagej.net/).

Modelling and simulation. Fully flexible force fields were developed for Ti, Zr, and Hf UiO-66 species. Specific parameters for all relevant interactions were derived from fits to ab initio data obtained for the reduced model as shown in Figure 2a. All ab initio calculations were carried out at the density functional theory (DFT) level with Gaussian09[29] using the wB97X-D functional[30] with the LANL2DZ basis set.[31] The atomic partial charges were calculated using the natural bond orbital (NBO) method.[32-34] After performing an energy optimization on the reduced model, potential energy scans were carried out to explore the global energy landscape. Fits to the potential energy curves were then performed with the genetic algorithm[35] to determine the force field parameters associated with the description of all bonds, angles, and dihedrals containing the metal centers. Specific details about the fitting procedure along with the complete list of the force field parameters are reported in the ESI. All molecular dynamics (MD) simulations were performed with DL POLY Classic[36] structures consisting of 1×1×1 primitive cells under periodic boundary conditions. The short-range interactions were truncated at an atom-atom distance of 9.0 Å, while the electrostatic interactions were treated using the Ewald method.[37] The system was equilibrated in the constant stress - constant temperature (NST) ensemble for 1 ns, which were then followed by additional 1 ns in the constant volume – constant temperature ensemble. The vibrational density of states was then calculated from subsequent 200 ps in the constant volume – constant energy (NVE) ensemble.
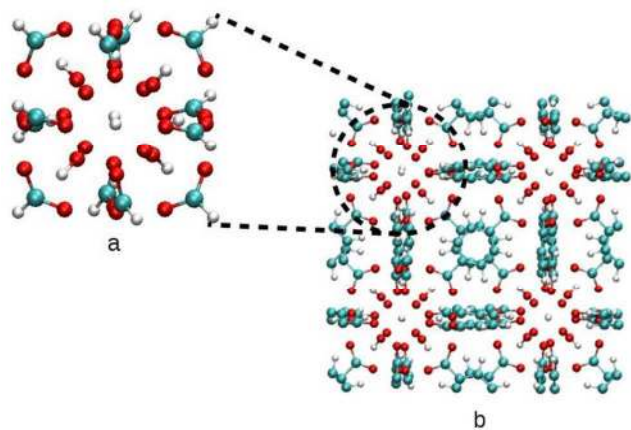

Figure 2. (a) Reduced and (b) expanded model for UiO-66(Hf).

RESULTS AND DISCUSSION

The original intention of this work was to study the PSE process of UiO-66(Zr) with exogenous metal ions via high-resolution STEM methods to elucidate the mechanism of this exchange process. We sought to learn the pathway and extent to which this exchange could be driven, whether PSE proceeded from the exterior to the interior of the particle, and what degree of PSE driven conversion would be tolerated by the MOF structure. In principle, complete exchange with Hf[4+] should be possible because UiO-

66(Hf) can be directly synthesized.[38] In contrast, the UiO-66(Ti) species has not been described. To address these questions, a series of MOF samples were subjected to both metal- and ligand-based PSE processes and analyzed by STEM imaging and spectroscopy.

UiO-66(Zr) particles were synthesized by standard protocols using an acetic acid modulator to yield monodisperse particles of ca. 100 nm. These particles were then subjected to PSE with HfCl4 and one of three Ti^{4+} sources: TiBr4, TiCp2Cl2, or TiCl4(THF)2. These exchange procedures were performed at 85 °C in DMF as previously described.[17] Exchange with TiCp2Cl2 was also performed at a higher temperature (120 °C) using both conventional and microwave heating conditions.[24] The resulting MOFs were characterized by PXRD, N2 sorption, TGA/DSC, and SEM-EDX analysis, giving results consistent with a PSE process (Figure 3). PXRD showed no obvious change in the crystallinity of the MOFs. N2 sorption analysis indicated that the porosity of the MOFs remained intact after PSE. Where a measurable BET surface area change was noted after PSE, the change in surface area was consistent with the expected PSE process, decreasing with the inclusion/addition of the heavier Hf[4+] ion and increasing with inclusion/addition of the lighter Ti^{4+} ions. The TiBr4 exchange sample shows an increase in sorptive capacity and BET surface area (ca. 1230 m²/g), while the HfCl4 exchange sample shows a decrease in both (ca. 960 m²/g), relative to the parent framework (ca. 1130 m²/g). Similarly, TGA-DSC analysis showed no behavior incongruent with a PSE process. The TiBr4 exchange sample shows a decrease in final residue mass, while the HfCl4 exchange sample shows an increase in final residue mass, relative to the parent framework, consistent with what would be expected for the exchange of lighter and heavier elements, respectively.
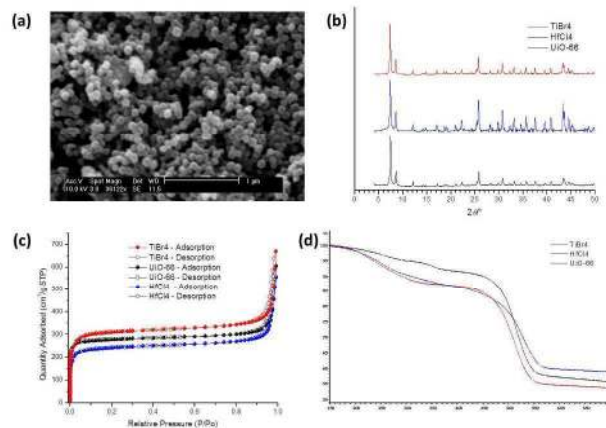
Figure 3. Characterization of MOFs after PSE. In each panel, data from the UiO-66(Zr) parent framework before PSE is shown in black, after exchange with HfCl4 at 85 °C for 5 d is shown in blue, and after exchange with TiBr4 at 85 °C for 5 d is shown in red. (a) Scanning electron micrograph of the as-synthesized UiO-66(Zr) particles. (b) PXRD data shows no notable change in crystallinity. (c) Gas sorption (N2) isotherm data show little change in surface area between samples. (d) TGA data shows only minor differences between samples.

Finally, SEM imaging shows that the particle size and shape are unchanged (Figures S10, S25) after PSE, within the limits of this imaging method. SEM-EDX analysis suggests incorporation/addition of the exogenous metal species. Following accepted protocols for calculating the extent of metal exchange, the percentages of exogenous species versus Zr[4+] were calculated for each sample using the total metals count from the EDX data. This

3

analysis shows the expected increase of the exogenous metal in the MOF sample as a function of reaction time over 1, 3, and 5 d (Figures S12, S19, S27, S34)

Unlike what is observable by SEM, TEM analysis revealed that the MOFs displayed distinct morphological differences before and after the PSE process. Despite the data presented in Figure 3 being consistent with a metal-based PSE process, STEM data revealed that there was clear deposition of a nanoscale coating on the particle exterior, not a true exchange process (**Error! Reference source not found.**). The coatings were determined to be a mix of amorphous and nanocrystalline deposits (Figure S21), several nanometers thick, with the underlying UiO-66(Zr) particle remaining single-crystalline. STEM-EDX atomic-percentage distribution maps (see ESI for analysis details) revealed that the nanoscale coatings are composed of the exogenous metal species intended for PSE. STEM EELS analysis reveals these coatings are oxygen rich and carbon deficient (Figure 5), suggesting that the coatings are oxides, namely TiO_2 or HfO_2. Moreover, particle mapping reveals that while there is an obvious deposition of the metal oxide on the surface of the particles, there is no evidence for the presence of metal exchange within the particle interior, which remains composed of Zr (Figure 4).

The as-synthesized UiO-66(Zr) particles (Figure 5a, Figure S78) are highly-crystalline with well resolved lattice fringes and sharp, clean edges. The averaged EDX spectrum generated from this sample (Figure 4c) shows only Zr peaks in addition to the expected C and O peaks (Cu 'system' peaks are also observed from microscope and grid). The spectra are consistent over all regions of the UiO-66(Zr) nanocrystals. Even when observed via low-magnification STEM imaging (Figure 4), the samples are clearly quite different morphologically after treatment with Hf^{4+} or Ti^{4+} at 85 °C for 5 d. The particle interiors still show resolvable lattice fringes with crystals not having significantly changed in size, but the particle surfaces show clear evidence of a non-uniform coating, or crust (Figure 5, Figure S78). After treatment with $HfCl_4$ this rough, largely amorphous hafnia surface coating on the particles is obvious in the Z-contrast STEM images. The STEM-EDX data collected for the samples help to explain this new morphology, and is essential to determine the elemental composition on the particles. STEM-EDX of the particle interior (Figure 4g, blue) revealed peaks characteristic of Zr only, while spectra collected at the particle surfaces (Figure 4g, red) contained strong characteristic peaks for Hf with a very low Zr signal. A similar surface coating, without exchange into the underlying parent particle is also observed for Ti-exchange species (**Error! Reference source not found.**h-k). STEM images (Figure 5h,i) and high-resolution (HR)TEM images (Figure S78b) clearly shows single crystalline particle-cores with amorphous and poly-crystalline coatings (anatase-TiO_2). Similarly, the STEM-EDX elemental mapping of Zr:Ti atomic ratio confirms the lack of Ti in the core of these particles (Figure 4n, blue), and the presence of highly Ti-rich surfaces (Figure 4n, red). All Ti-samples (using several different Ti-salts) display rough surfaces after PSE processing, and all have the characteristic Ti-rich surface coating over the Zr-core in their EDX spectral maps (Figure S43).
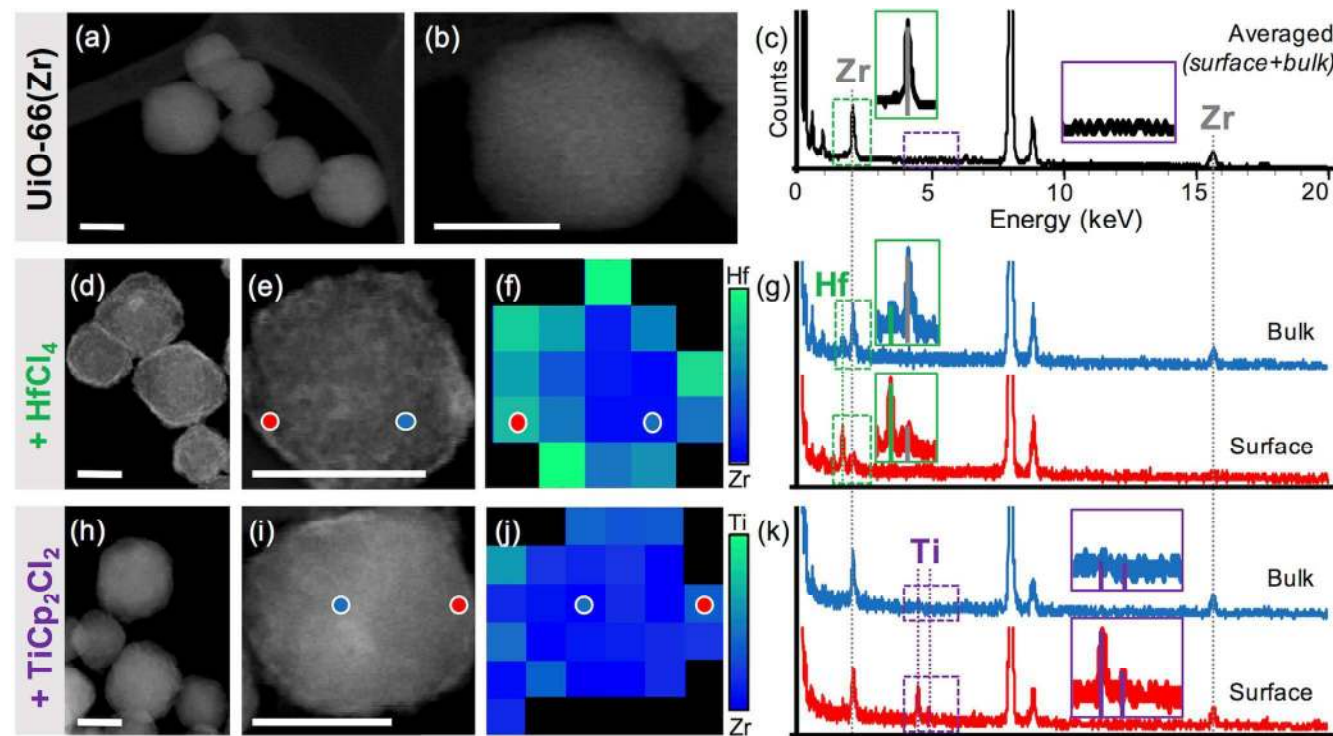
Figure 4. STEM-EDX characterization for UiO-66(Zr), UiO-66(Zr)+$HfCl_4$, or UiO-66(Zr)+$TiCp_2Cl_2$. All scale bars are 50 nm. STEM images of low- (a, d, h) and high-magnification (b, e, i) are shown for each sample. STEM-EDX spectra are provided (c, g, k). (f) STEM-EDX Hf:Zr atomic ratio map for UiO-66(Zr)+$HfCl_4$ in panel (e). (g) STEM-EDX spectra for UiO-66(Zr)+$HfCl_4$ from the surface (red) and interior (blue) regions (the red and blue dots in panels (e, f) indicate where these spectra where acquired). (j) STEM-EDX Hf:Ti atomic ratio map for UiO-66(Zr)+$TiCp_2Cl_2$ in panel (i). (k) STEM-EDX spectra for UiO-66(Zr)+$TiCp_2Cl_2$ from the surface (red) and interior (blue) regions (the red and blue dots in panels (i, j) indicate where these spectra where acquired).

Given that these findings suggest that reinterpretation of literature pertaining to metal PSE in UiO-66 is required, other previously reported PSE procedures (beyond incubation at 85 °C for 5 d) were examined. Specifically, Tu et al.[24] used higher temperatures (120 °C vs. 85 °C) and microwave heating to achieve PSE in UiO-66(Zr) in a shorter time (hours vs. days). Following the pub-

4

lished protocol, the UiO-66(Zr) particles were heated with $TiCp_2Cl_2$ in DMF for 3 h in a microwave reactor (Figure S43). The STEM data here show an even thicker surface coating on the particles (Figure S43) than for conventional heating described above. The greater deposition on the particles is consistent with the higher apparent Ti incorporation described in the original report.[24] EDX spectral mapping confirms Ti present only on the particle surface and not in the interior, which remains composed of Zr. A control experiment was performed using conventional heating at 120 °C for 24 h, giving results consistent with heating at 85° C, but with thicker surface layers.

STEM images and STEM-EDX data show that there is deposition of a Ti- or Hf-containing species on the particle surfaces and there is no metal exchange in the particle interiors. Therefore, we sought to confirm that the metals were being deposited from solutions as metal oxides, rather than metal carbides or MOF-like structures. To confirm the STEM-EDX results, analysis of light elements, namely carbon and oxygen, were needed, as an oxide deposition would be rich in oxygen, but poor in carbon (unlike a MOF phase, which has both oxygen and carbon from the organic ligands). EDX analysis has poor sensitivity for these low-Z species, especially carbon, so we employed STEM electron-energy loss spectroscopy (EELS) elemental mapping and ICP-MS to determine the complete elemental composition of these surface layers and the composition of any species extracted from the particles.

STEM-EELS mapping of the particle surfaces provides strong evidence of the deposition of metal oxides on the particle surface (Figure 5). STEM-EELS is an ideal complementary nanoscale elemental mapping technique to STEM-EDX, as it is extremely sensitive to low-Z elements. High-resolution maps of C and O content on the particle edges were generated using STEM-EELS for the parent UiO-66(Zr) particles and for the Hf- and Ti- PSE particles (Figure 5). In the case of the Ti-PSE particles, the Ti signal was also clearly identified and mapped (Figure 5). Detection of Hf in Hf-PSE particles was also achieved by EELS, though these spectral maps are not shown in the manuscript due to the low signal-to-noise at the high energy loss region of the EELS spectra). In the native UiO-66, both C and O are present in uniform relative concentrations out to the particle surface, indicating an intact crystal containing the bdc^{2-} ligand throughout (**Error! Reference source not found.**c, d). Specifically, strong and consistent C signal is found up to the crystalline surface. Oxygen also extends to the surface, but as the O atomic percent composition is lower than C in bdc^{2-}, the O signal more noticeably tapers off towards the surface.

In both the Hf-and Ti-exchanged samples, the rough surface deposits show very little C in the deposited layer, significantly less than at the surface of the pristine UiO-66, which certainly contain bdc^{2-} at the surface. However, in both exchanged samples, very high O concentration is found in these surface layers, matching very well with the deposition layer region in the STEM images (**Error! Reference source not found.**). These data are consistent with the hypothesis that the exogenous metal is being deposited as a metal oxide coating, which would be rich in O and deficient in C, and not as a ligand-rich MOF framework, which would be reversed in C/O content. The Ti elemental map of the Ti-PSE particle in Figure 5l indicates the presence of Ti located at the surface of the particle, and co-localized with the O-rich and C-deficient region. Taken together with the STEM-EDX data, which shows both the Hf and Ti exogenous metals in the surface deposited regions, these EELS data give a consistent picture of a nanoscale surface coating of a-HfO_x/HfO_2 or a-TiO_x/TiO_2, respectively.
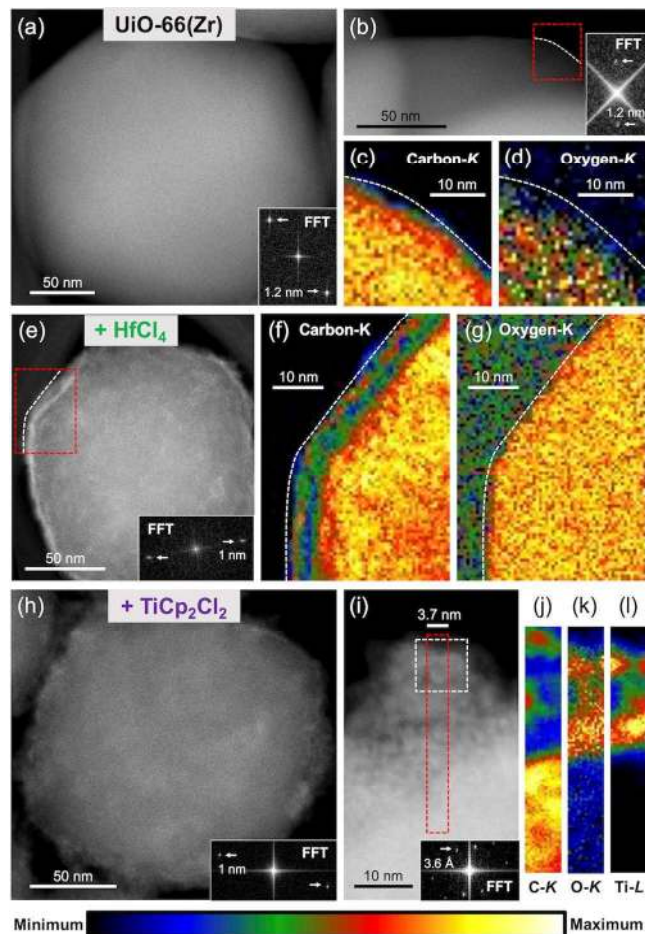

Figure 5. STEM-EELS characterization of: (a-d) UiO-66(Zr), (e-g) UiO-66(Zr)+$HfCl_4$, or (h-l) UiO-66(Zr)+$TiCp_2Cl_2$. (a, e, h) HAADF STEM images, where insets of the Fast Fourier Transform (FFT) of each image show in the interior of the particles (111) or (002) fringes of UiO-66(Zr) observed at ~1.2 and 1 nm, respectively. Only for UiO-66(Zr) do these lattice fringes extend to the particle surface. (c, d) STEM-EELS spectral maps of Carbon-K and Oxygen-K for a region of the UiO-66(Zr) sample marked by the red box in panel (b). (f, g) STEM-EELS spectral maps of Carbon-K and Oxygen-K for a region of the UiO-66(Zr)+$HfCl_4$ sample marked by the red box in panel (e). (j-l) STEM-EELS spectral maps of Carbon-K, Oxygen-K, and Titanium-$L2,3$ for a region of the UiO-66(Zr)+$TiCp_2Cl_2$ sample marked by the red box in panel (i). Color bar at the bottom indicates the EELS mapping of relative signal intensity.

If some form of metal PSE were occurring, Zr^{4+} should be liberated into solution as the ions are displaced by the incoming metal ions. In a PSE process, increasing exogenous metal content in the MOF particles should correspond to decreasing exgenous metal-content and increasing Zr-content in the supernatant. Alternatively, for a metal-oxide deposition process, Zr would not be liberated, and should not be found in the supernatant. ICP-MS analysis of both the MOF particles after PSE and the PSE supernatant was performed to determine the content of Hf, Ti, and Zr present in the particles and solutions (Figure 6).

ICP-MS analysis of the MOF particles after PSE shows the same trend of metal-inclusion as SEM-EDX data, indicating that the MOFs do contain the exogenous metals and the amount of exogenous metal increases with longer incubation times (Figure 6). In fact, when plotted as atomic percentage, i.e. [(moles Ti)/(moles Ti + moles Zr)]*100%), both SEM-EDX and ICP-MS

1
2
3
4
5
6
7
8
9
10
11
12
13
14
15
16
17
18
19
20
21
22
23
24
25
26
27
28
29
30
31
32
33
34
35
36
37
38
39
40
41
42
43
44
45
46
47
48
49
50
51
52
53
54
55
56
57
58
59
60

data show increasing exogenous metal in the MOF particles during incubation (Figures S12, S13, S19, S20, S27, S28, S34, S35). The ICP-MS data on the MOF particles is consistent with the expected PSE mechanism, in that, the atomic percent of exogenous metal in the MOF increases, while the Zr amount appears to decrease. However, an alternative explanation is that the exogenous metal is simply depositing on the particles, which would result in a similar increase in HF/Ti signal and an apparent reduction in the atomic percent of Zr, as observed. Therefore, ICP-MS on the MOF particles alone is insufficient to distinguish between PSE and metal oxide deposition processes.

Importantly, on examination of the exchange reaction supernatant by ICP-MS, the STEM-EDX and STEM-EELS are confirmed. The amount Hf or Ti in solution drops over time, but there is no corresponding amount of Zr found in the supernatant (Figure 6). The lack of Zr being displaced from the sample into solution is a clear indicator that PSE is not proceeding as assumed.
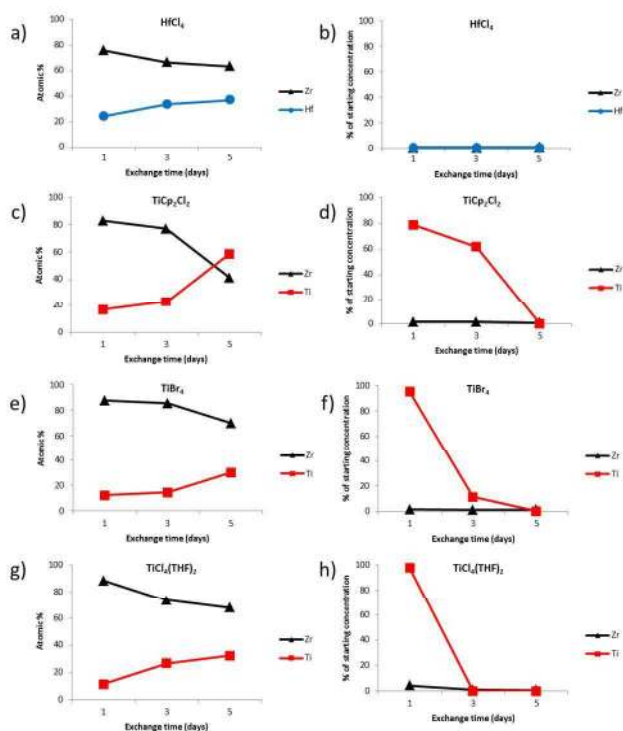
Figure 6. ICP-MS data showing Zr, Ti, and Hf amounts in PSE processed samples: (a, c, e, f) digested MOFs after PSE, and (b, d, f, h) reaction supernatants after PSE.

To determine if metal exchange is possible in UiO-66(Hf), PSE with Zr^{4+} was attempted. Once again, the data from the standard suite of MOF characterization methods appears to indicate the partial exchange of Zr for Hf. The PXRD shows high MOF crystallinity (Figure S49), SEM-EDX and ICP-MS of the particles show Zr inclusion (Figures S53, S54), and N_2 isotherm data show an increase in capacity and surface area consistent with substitution of Zr for Hf (Figure S50). In the absence of other data, metal PSE on this sample would be a reasonable conclusion, but analysis by STEM-EDX (Figure 7) and ICP-MS of the supernatant reveal metal oxide deposition. By STEM imaging, the particles show a rough surface coating, where the as-prepared UiO-66(Hf) have pristine surfaces much like the as-prepared UiO-66(Zr). Furthermore, STEM-EDX elemental maps indicate that the Zr is only present at the surface of the particle, with Hf found solely in the core (Figure 7). ICP-MS of the supernatant shows that Zr is

steadily depleted from solution, but shows that no Hf is present in the supernatant over the course of 5 days (Figure S54).
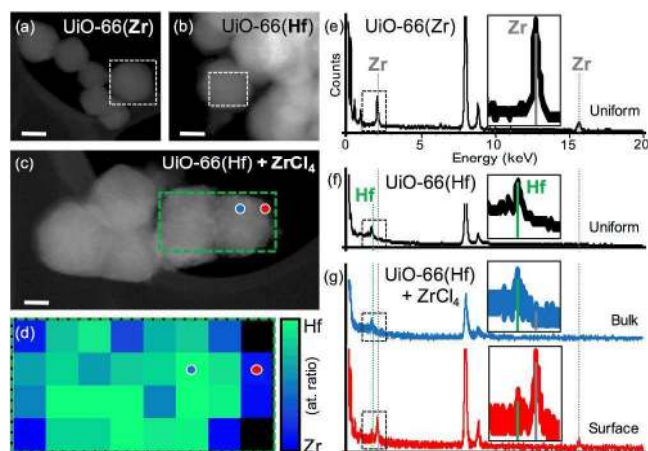
Figure 7. HAADF STEM images of (a) UiO-66(Zr), (b) UiO-66(Hf), and (c) UiO-66(Hf) + ZrCl$_4$. All scale bars are 50 nm. (d) STEM-EDX Hf:Zr atomic ratio map for the UiO-66(Hf) + ZrCl$_4$ sample over the region indicated by the green box in (c). (e) STEM-EDX averaged-spectra for the UiO-66(Zr) particle indicated by the white box in (a). (f) STEM-EDX averaged-spectra for the UiO-66(Hf) particle indicated by the white box in (b). (g) Two individual STEM-EDX spectra for the UiO-66(Hf) + ZrCl$_4$ particle mapped in (f), one from the surface region of that particle (red), and one from the bulk region (core) that particle (blue). The red and blue dots in (c,d) indicate the location where these spectra where acquired. Insets in (e-g) magnify the region of these spectra indicated by the black dashed rectangles.

Computational modelling was employed to determine if metal PSE is thermodynamically feasible. The unit cell parameters and all metal-oxygen distances for UiO-66(Ti), UiO-66(Zr), and UiO-66(Hf) obtained from the NST simulations are compared with the available experimental data and previous DFT calculations (Table 1, Table 2).[39-40] In all cases, good agreement is found with both experimental and simulation values reported in the literature. The vibrational densities of states are quite similar for all the three MOFs and, in the case UiO-66(Zr), consistent with the results reported previously from ab initio molecular dynamics simulations (Figure 8).[41] The peak at 3738 cm^{-1} corresponds to the OH stretching frequency of μ_3-OH. This value agrees with results obtained from ab initio molecular dynamics simulations (3731 cm^{-1}) and experimental measurements (3676 cm^{-1}).[41] The CH stretching frequencies of the aromatic bdc^{2-} ligands are located at 3134 cm^{-1} and the frequencies between 400 and 1638 cm^{-1} are associated with the intramolecular motion of the organic ligands, corresponding to the ring out-of-plane vibrations and distortions and C–C stretches. Vibrations of the Zr$_6$-octahedron units are found between 400–470 and 650–850 cm^{-1}.[41] Other lower frequencies are associated with the carboxylate torsion and other global modes of the organic ligands.

Table 1. Cubic lattice parameters for UiO-66(Ti), UiO-66(Zr), and UiO-66(Hf).

| MOF	Lattice parameters ($a = b = c$, Å)	
	Simulation	Experiment
UiO-66(Hf)	20.97	20.7[38]
UiO-66(Zr)	20.93	20.978[40, 42]
UiO-66(Ti)	21.16	-

6

Table 2. Metal-oxygen distances for UiO-66(Ti), UiO-66(Zr), and UiO-66(Hf).

Metal-oxygen bond	Bond distance (Å)		
	DFT[39]	Simulation	Experiment
Hf-o	2.22	2.41	-
Hf- oh	2.25	2.27	-
Hf-os	2.06	2.20	-
Zr-o	2.25	2.37	2.22[40]
Zr-oh	2.28	2.34	2.26[40]
Zr-os	2.09	2.19	2.06[40]
Ti-o	2.25	2.42	-
Ti-oh	2.28	2.31	-
Ti-os	2.08	2.21	-

From the vibrational densities of state, the Helmholtz free energies were calculated within the quasi-harmonic approximation, according to:

$$F = U_{conf} + \frac{1}{2}\int D\,(\nu)h\nu d\nu + k_B T \int ln\left(1 - exp\left(\frac{-h\nu}{K_B T}\right)\right)$$

where U_{conf} is the potential energy and $D(\nu)$ is the vibrational density of state as a function of vibrational frequency, ν. The Helmholtz free energies of UiO-66(Ti), UiO-66(Zr), and UiO-66(Hf) MOFs are reported in Table 3. The theoretical estimates demonstrate the UiO-66(Hf) has the lowest free energy, followed by UiO-66(Zr) and UiO-66(Ti). Based on this thermodynamic analysis, it is thus possible to envision metal exchange between Zr and Hf; however, as shown above, alternative pathways may preclude the PSE process from occurring. On the other hand, the higher free energy for UiO-66(Ti) indicates that it is not thermodynamically favorable to exchange Zr with Ti, which is consistent with the lack of reports on the synthesis of UiO-66(Ti).
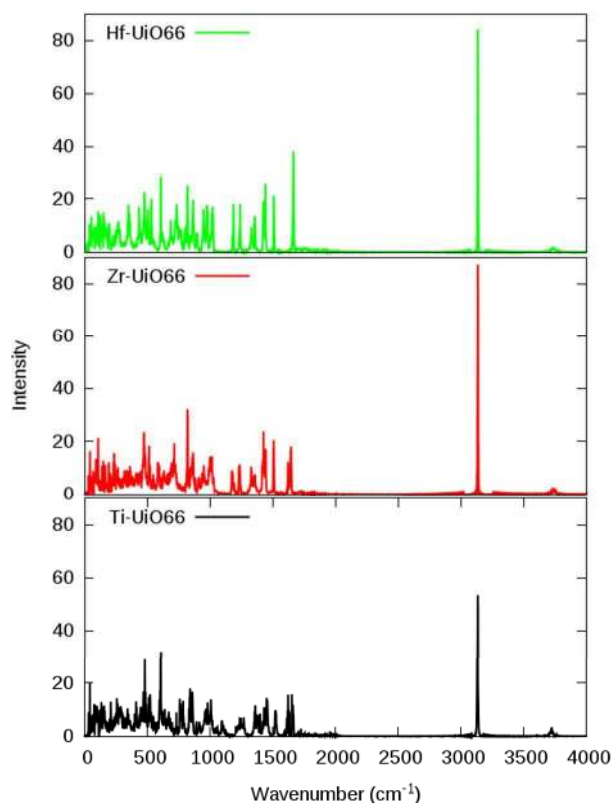
Figure 8. The density of states calculated from the Fourier transform of the atomic velocities autocorrelation function is represented as a function of wavenumber for UiO-66(Ti), UiO-66(Zr), and UiO-66(Hf).

Importantly, although metal-based PSE with Ti and Hf does not occur, ligand-based PSE in the UiO-66(Zr) system was confirmed, consistent with previous crystallographic reports.[43] Using reported procedures, both 2-bromoterephthalic acid (Br-H$_2$bdc) and 2-iodoterephthalic acid (I-H$_2$bdc) were incorporated into UiO-66(Zr) at room temperature and their presence both on the particle exterior and interior was confirmed by STEM-EDX (Figure 9). In stark contrast to the metal-based PSE samples, the particle surfaces during ligand PSE remain sharp and clean in STEM images, and both Br and I signals are observable in uniform concentrations over the EDX map of a single particle. We note that accurate quantification of Br atomic percentage by EDX was problematic due to the Br peak location, which is at low energy, within the background, such that the Br peak is partially removed when applying the background subtraction that is necessary for EDX quantification. This makes computed atomic percent in Figure 9k artificially low, and the true atomic % cannot be accurately determined. However, a clear Br peak, such as the one seen in Figure 9l is present in each of the nine spectra used to generate the Br map (strong Br signal at all regions of the particle). This evidence of ligand PSE is further supported by ^{1}H NMR analysis of the digested MOF samples and the PSE supernatant (Figures S58, S59, S63, S64). The ^{1}H NMR spectra confirm that the exogenous ligand is incorporated into the MOF particles and native bdc^{2-} is being displaced into the supernatant in complementary levels to exogenous ligand incorporation.

Finally, to validate the STEM-EDX technique for monitoring metal PSE in MOFs, a system that has been unambiguously confirmed to undergo metal-based PSE by single crystal X-ray diffraction and optical spectroscopy was evaluated by STEM (Figure 10). A sample of a Zn-based MOF reported by the Zou[44] and Lah labs[45] was subjected to metal PSE with Cu^{2+}. By SEM-EDX, the exchange particles show complete conversion to the Cu-species (Figures S67, S72), which was confirmed by ICP-MS of the digested particles (Figure S73). Unlike UiO-66(Zr), ICP-MS of the exchange supernatant shows the presence of dissolved Zn in a nearly identical molar quantity to the amount of Cu exchanged into the particles (Figure S74). Finally, STEM showed that these particles had similarly porous surfaces to the pre-exchange Zn-MOF particles, and STEM-EDX elemental mapping confirms a uniform composition of Cu throughout the entire particle, with essentially no Zn detected in the sample after incubation with Cu(NO$_3$)$_2$, consistent with a true metal PSE process (Figure 10).

Table 3. Calculated energies for each MOF species.

MOF	Potential energy/unit cell	Vibrational and entropic energy	Free energy (Kcal/mol)
UiO-66(Ti)	-1671.18	-852.53	-2436.78
UiO-66(Zr)	-2406.58	-841.38	-3247.96
UiO-66(Hf)	-3595.82	-880.35	-4476.17

7
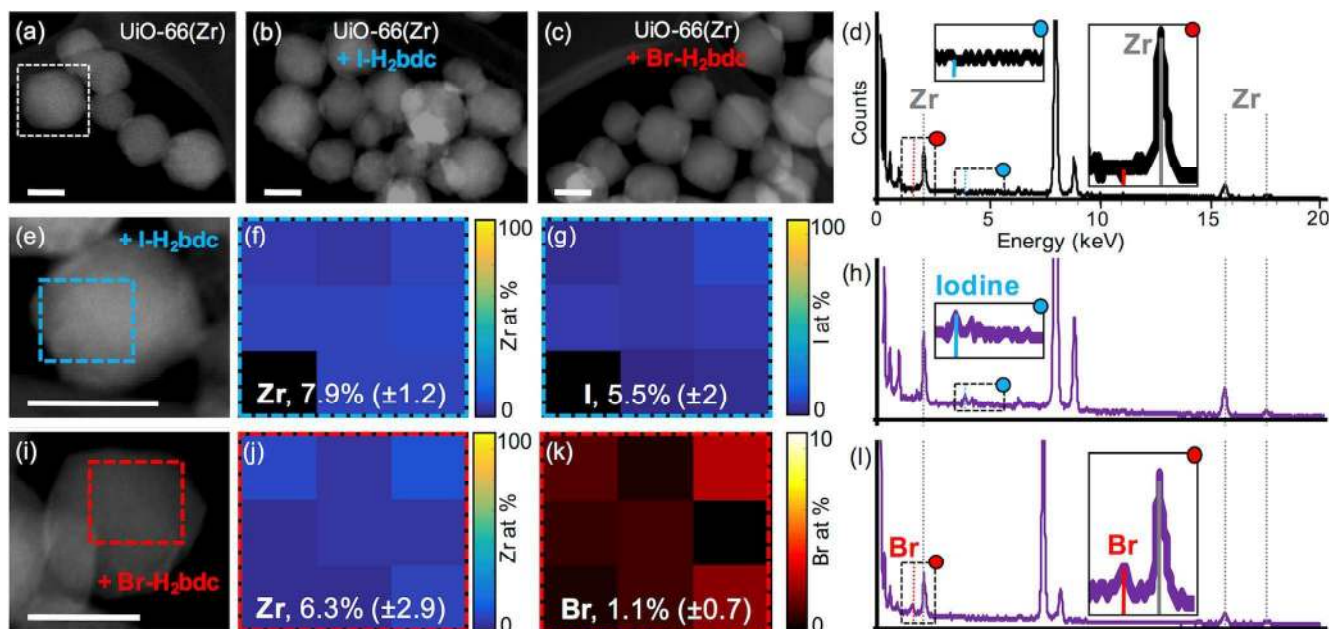
Figure 9. STEM-EDX characterization of (a, d) UiO-66(Zr), and UiO-66(Zr) incubated with (b, e-h) I-H$_2$bdc or (c, i-l) Br-H$_2$bdc. All scale bars are 50 nm. HAADF STEM images of (a) UiO-66(Zr), (b) UiO-66(Zr) + I-H$_2$bdc, and (c) UiO-66(Zr) + Br-H$_2$bdc. (d) STEM-EDX averaged-spectra for the UiO-66(Zr) particle indicated by the white box in panel (a). (e) HAADF STEM image of one UiO-66(Zr) + I-H$_2$bdc particle selected for EDX analysis. STEM-EDX atomic percent map for Zr (f) and I (g) for the region indicated by the blue box in panel (e). (h) STEM-EDX averaged-spectra for the region indicated by the blue box in panel (e) averaged from eight spectra. (i) HAADF STEM image of one UiO-66(Zr) + Br-H$_2$bdc particle selected for EDX analysis. STEM-EDX Zr (j) and Br (k) for the region indicated by the red box in panel (i). (l) STEM-EDX averaged-spectra for the region indicated by the red box in panel (i) averaged from nine spectra. The EDX maps show uniform distribution of the I and Br signals in the respective samples confirming uniform ligand PSE in the samples.
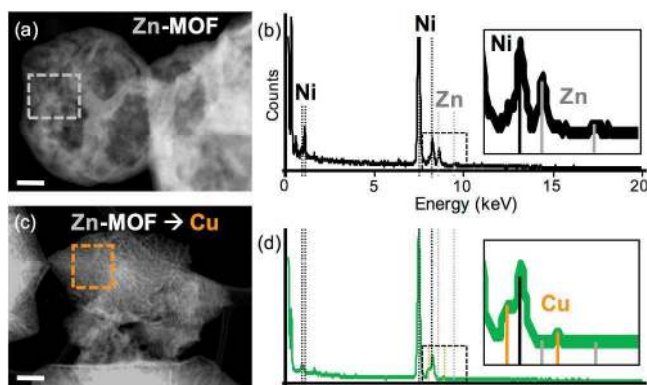
Figure 10. STEM-EDX characterization of Zn-MOF and Zn-MOF incubated with Cu(NO$_3$)$_2$. All scale bars are 50 nm. (a) HAADF STEM image and (b) STEM-EDX averaged-spectra for the region indicated by the grey box of a Zn-MOF particle. (c) HAADF STEM image and (d) STEM-EDX averaged-spectra for the region indicated by the orange box of a Zn-MOF particle exchanged with Cu(NO$_3$)$_2$. These data confirm uniform, complete displacement of Zn for Cu in this MOF.

CONCLUSIONS

By employing analytical STEM methods and supernatant analysis by ICP-MS, we have concluded that the incubation of UiO-66(Zr) with Ti and Hf sources results in the deposition of nanoscale metal oxide coatings on the particles and not metal-based PSE as had been previously reported. High-resolution STEM techniques revealed that the exogenous metal is localized to the deposited surface material in the final product, and supernatant analysis

confirms that while the exogenous metal is depleted during incubation, no Zr is displaced from the MOF. Curiously, these metal oxide coatings do not block MOF porosity. This procedure of incubation of UiO-66 with metal sources then, should be understood not as PSE, but instead as a route to creating novel metal oxide@UiO-66 core-shell composite materials. Understanding the structure of these products is important for several reasons. First, it helps to explain the well documented enhanced catalytic activity of these composites, especially in photocatalytic systems. The photocatalytic activity of nanoscale TiO$_2$ is well known. [46-48] We can accurately describe the above results as a route to generating nano-TiO$_2$ supported on a porous substrate. This composite is likely to be highly useful for many catalytic transformations, and understanding the correct structure of this material will allow for further catalytic optimization. Similarly, we would urge that reports of metal-based PSE in UiO-66 be reinterpreted through the lens of this MOF@metal oxide structure. With access to a core-shell MOF@metal oxide structure, the range of nanoscale metal oxide species that can form on the surface of UiO-66 and the utility of such composites will be an area of fruitful exploration. As a final point, we believe this work presents a strong case for careful attention to complete analysis of MOF materials. Observation of these materials at length scales accessible to STEM led to a new understanding of this system. For systems where PSE is assumed to be occurring, electron microscopy should be employed because of the unparalleled information it can give about MOF nanostructure.

Supporting Information

The Supporting Information is available free of charge on the ACS Publications website. Experimental details and additional data (PDF), including synthetic protocols and materials characterization.

AUTHOR INFORMATION

Corresponding Author

*scohen@ucsd.edu; nathan.gianneschi@northwestern.edu

Author Contributions

†These authors contributed equally to this work.

Notes
The authors declare no competing financial interests.

ACKNOWLEDGMENT

REFERENCES

1. Gangu, K. K.; Maddila, S.; Mukkamala, S. B.; Jonnalagadda, S. B., *Inorg. Chim. Acta*, **2016,** *446*, 61-74.
2. Furukawa, H.; Cordova, K. E.; O'Keeffe, M.; Yaghi, O. M., *Science*, **2013,** *341*.
3. Li, B.; Wen, H.-M.; Cui, Y.; Zhou, W.; Qian, G.; Chen, B., *Adv. Mater.*, **2016,** *28*, 8819-8860.
4. Wang, H.; Zhu, Q.-L.; Zou, R.; Xu, Q., *Chem*, **2017,** *2*, 52-80.
5. Huang, Y.-B.; Liang, J.; Wang, X.-S.; Cao, R., *Chem. Soc. Rev.*, **2017,** *46*, 126-157.
6. Zeng, L.; Guo, X.; He, C.; Duan, C., *ACS Catal.*, **2016,** *6*, 7935-7947.
7. Zhu, L.; Liu, X.-Q.; Jiang, H.-L.; Sun, L.-B., *Chem. Rev.*, **2017,** *117*, 8129-8176.
8. Farrusseng, D.; Aguado, S.; Pinel, C., *Angew. Chem. Int. Ed.*, **2009,** *48*, 7502-7513.
9. Wang, Z.; Cohen, S. M., *Chem. Soc. Rev.*, **2009,** *38*, 1315-1329.
10. Islamoglu, T.; Goswami, S.; Li, Z.; Howarth, A. J.; Farha, O. K.; Hupp, J. T., *Acc. Chem. Res.*, **2017,** *50*, 805-813.
11. Cohen, S. M., *Chem. Rev.*, **2012,** *112*, 970-1000.
12. Marshall, R. J.; Forgan, R. S., *Eur. J. Inorg. Chem.*, **2016,** *2016*, 4310-4331.
13. Evans, J. D.; Sumby, C. J.; Doonan, C. J., *Chem. Soc. Rev.*, **2014,** *43*, 5933-5951.
14. Deria, P.; Mondloch, J. E.; Karagiaridi, O.; Bury, W.; Hupp, J. T.; Farha, O. K., *Chem. Soc. Rev.*, **2014,** *43*, 5896-5912.
15. Brozek, C. K.; Dinca, M., *Chem. Soc. Rev.*, **2014,** *43*, 5456-5467.
16. Cavka, J. H.; Jakobsen, S.; Olsbye, U.; Guillou, N.; Lamberti, C.; Bordiga, S.; Lillerud, K. P., *J. Am. Chem. Soc.*, **2008,** *130*, 13850-13851.
17. Kim, M.; Cahill, J. F.; Fei, H.; Prather, K. A.; Cohen, S. M., *J. Am. Chem. Soc.*, **2012, **134*, 18082-18088.
18. Smith, S. J. D.; Ladewig, B. P.; Hill, A. J.; Lau, C. H.; Hill, M. R., *Sci. Rep.*, **2015,** *5*, 7823.
19. Hon Lau, C.; Babarao, R.; Hill, M. R., *Chem. Commun.*, **2013,** *49*, 3634-3636.
20. Ye, G.; Qi, H.; Li, X.; Leng, K.; Sun, Y.; Xu, W., *Chemphyschem*, **2017,** *18*, 1903-1908.
21. Rasero-Almansa, A. M.; Iglesias, M.; Sanchez, F., *RSC Adv.*, **2016,** *6*, 106790-106797.
22. Sun, D.; Liu, W.; Qiu, M.; Zhang, Y.; Li, Z., *Chem. Commun.*, **2015,** *51*, 2056-2059.
23. Nguyen, H. G. T.; Mao, L.; Peters, A. W.; Audu, C. O.; Brown, Z. J.; Farha, O. K.; Hupp, J. T.; Nguyen, S. T., *Catal. Sci. Technol.*, **2015,** *5*, 4444-4451.
24. Tu, J.; Zeng, X.; Xu, F.; Wu, X.; Tian, Y.; Hou, X.; Long, Z., *Chem. Commun.*, **2017,** *53*, 3361-3364.
25. Lee, Y.; Kim, S.; Kang, J. K.; Cohen, S. M., *Chem. Commun.*, **2015,** *51*, 5735-5738.
26. Santaclara, J. G.; Olivos-Suarez, A. I.; Gonzalez-Nelson, A.; Osadchii, D.; Nasalevich, M. A.; van der Veen, M. A.; Kapteijn, F.; Sheveleva, A. M.; Veber, S. L.; Fedin, M. V.; Murray, A. T.; Hendon, C. H.; Walsh, A.; Gascon, J., *Chem. Mater.*, **2017**.
27. Zhu, Y.; Ciston, J.; Zheng, B.; Miao, X.; Czarnik, C.; Pan, Y.; Sougrat, R.; Lai, Z.; Hsiung, C. E.; Yao, K.; Pinnau, I.; Pan, M.; Han, Y., *Nat. Mater.*, **2017,** *16*, 532-536.
28. Patterson, J. P.; Abellan, P.; Denny, M. S.; Park, C.; Browning, N. D.; Cohen, S. M.; Evans, J. E.; Gianneschi, N. C., *J. Am. Chem. Soc.*, **2015,** *137*, 7322-7328.
29. M. J. Frisch, G. W. T., H. B. Schlegel, G. E. Scuseria, M. A. Robb, J. R. Cheeseman, G. Scalmani, V. Barone, G. A. Petersson, H. Nakatsuji, X. Li, M. Caricato, A. Marenich, J. Bloino, B. G. Janesko, R. Gomperts, B. Mennucci, H. P. Hratchian, J. V. Ortiz, A. F. Izmaylov, J. L. Sonnenberg, D. Williams-Young, F. Ding, F. Lipparini, F. Egidi, J. Goings, B. Peng, A. Petrone, T. Henderson, D. Ranasinghe, V. G. Zakrzewski, J. Gao, N. Rega, G. Zheng, W. Liang, M. Hada, M. Ehara, K. Toyota, R. Fukuda, J. Hasegawa, M. Ishida, T. Nakajima, Y. Honda, O. Kitao, H. Nakai, T. Vreven, K. Throssell, J. A. Montgomery, Jr., J. E. Peralta, F. Ogliaro, M. Bearpark, J. J. Heyd, E. Brothers, K. N. Kudin, V. N. Staroverov, T. Keith, R. Kobayashi, J. Normand, K. Raghavachari, A. Rendell, J. C. Burant, S. S. Iyengar, J. Tomasi, M. Cossi, J. M. Millam, M. Klene, C. Adamo, R. Cammi, J. W. Ochterski, R. L. Martin, K. Morokuma, O. Farkas, J. B. Foresman, and D. J. Fox. Gaussian09. Gaussian, Inc., Wallingford, CT, USA, 2009.
30. Chai, J.-D.; Head-Gordon, M., *Phys. Chem. Chem. Phys.*, **2008,** *10*, 6615-6620.
31. Hay, P. J.; Wadt, W. R., *J. Chem. Phys.*, **1985,** *82*, 299-310.
32. Foster, J. P.; Weinhold, F., *J. Am. Chem. Soc.*, **1980,** *102*, 7211-7218.
33. Reed, A. E.; Weinhold, F., *J. Chem. Phys.*, **1983,** *78*, 4066-4073.
34. Reed, A. E.; Weinstock, R. B.; Weinhold, F., *J. Chem. Phys.*, **1985,** *83*, 735-746.
35. Goldberg, D. E., *Genetic Algorithms in Search, Optimization and Machine Learning*. Addison-Wesley Longman Publishing Co., Inc.: Boston, MA, 1989; p 372.

9

36. Smith, W. F., T.; Todorov, I. . The DL POLY Classic User Manual. STFC Daresbury Laboratory Daresbury, Warrington WA4 4AD Cheshire, UK, 2010.

37. Leach, A. R., *Molecular Modeling: Principles and Applications*. 2nd ed.; Pearson Prentice Hall: Harlow, England, 2001.

38. Jakobsen, S.; Gianolio, D.; Wragg, D. S.; Nilsen, M. H.; Emerich, H.; Bordiga, S.; Lamberti, C.; Olsbye, U.; Tilset, M.; Lillerud, K. P., *Phys. Rev. B*, **2012,** *86*, 125429.

39. Yang, L.-M.; Ganz, E.; Svelle, S.; Tilset, M., *J. Mater. Chem. C*, **2014,** *2*, 7111-7125.

40. Bristow, J. K.; Svane, K. L.; Tiana, D.; Skelton, J. M.; Gale, J. D.; Walsh, A., *J. Phys. Chem. C, Nanomater. Interfaces*, **2016,** *120*, 9276-9281.

41. Van Yperen-De Deyne, A.; Hendrickx, K.; Vanduyfhuys, L.; Sastre, G.; Van Der Voort, P.; Van Speybroeck, V.; Hemelsoet, K., *Theor. Chem. Acc.*, **2016,** *135*, 102.

42. Yang, Q.; Guillerm, V.; Ragon, F.; Wiersum, A. D.; Llewellyn, P. L.; Zhong, C.; Devic, T.; Serre, C.; Maurin, G., *Chem. Commun.*, **2012,** *48*, 9831-9833.

43. Oien-Odegaard, S.; Braglia, L.; Lamberti, C.; Lillerud, K. P., Direct Probing of Postsynthetic Modifications in Zr-MOF Single Crystals. In *MOF 2016*, Long Beach, CA, 2016.

44. Yao, Q.; Sun, J.; Li, K.; Su, J.; Peskov, M. V.; Zou, X., *Dalton Trans.*, **2012,** *41*, 3953-3955.

45. Song, X.; Kim, T. K.; Kim, H.; Kim, D.; Jeong, S.; Moon, H. R.; Lah, M. S., *Chem. Mater.*, **2012,** *24*, 3065-3073.

46. Nakata, K.; Fujishima, A., *J. Photoch. Photobio. C*, **2012,** *13*, 169-189.

47. Schneider, J.; Matsuoka, M.; Takeuchi, M.; Zhang, J.; Horiuchi, Y.; Anpo, M.; Bahnemann, D. W., *Chem. Rev.*, **2014,** *114*, 9919-9986.

48. Rao, T. N.; Tryk, D. A.; Fujishima, A., Applications of TiO2 Photocatalysis. In *Encyclopedia of Electrochemistry*, Wiley-VCH Verlag GmbH & Co. KGaA: Hoboken, NJ, 2007.

1
2
3
4
5
6
7
8
9
10
11
12
13
14
15
16
17
18
19
20
21
22
23
24
25
26
27
28
29
30
31
32
33
34
35
36
37
38
39
40
41
42
43
44
45
46
47
48
49
50
51
52
53
54
55
56
57
58
59
60

10